Article

Not peer-reviewed version

Analysis, Design, and Experimental Validation of a High-Isolation, LowCross-Polarization Antenna Array Demonstrator for Software-Defined-Radar Applications

Nicholas Ricciardella , Walter Fuscaldo , Tito Mattei , Anna Maria Fiorello , Leopoldo Infante ,
Alessandro Galli *

Posted Date: 28 May 2024

doi: 10.20944/preprints202405.1892.v1

Keywords: phased arrays; planar arrays; antenna radiation patterns; beam steering; radar antennas; radar applications

Article

Analysis, Design, and Experimental Validation of a High-Isolation, Low Cross-Polarization Antenna Array Demonstrator for Software-Defined-Radar Applications

Nicholas Ricciardella [1,†], Walter Fuscaldo [2,†,‡], Tito Mattei [1,†], Anna Maria Fiorello [1,†], Leopoldo Infante [1,†] and Alessandro Galli [3,†]

[1] Electronics Division Leonardo SpA, 00131 Rome, Italy
[2] Consiglio Nazionale delle Ricerche, Istituto per la Microelettronica e Microsistemi, 00133 Rome, Italy
[3] Dept. of Information Engineering, Electronics and Telecommunications, Sapienza University of Rome, 00184 Rome, Italy
‡ walter.fuscaldo@cnr.it
‡ These authors contributed equally to this work.

Abstract: In a software-defined radar (SDR) system, most of the signal processing usually implemented in hardware is implemented by software, thus allowing for higher flexibility and modularity compared to conventional radar systems. However, the majority of SDR demonstrators and proofs-of-concept reported in the open literature so far have been based on simple antenna systems. As a result, the full potentialities of an SDR approach have not been completely exploited yet. In this work, we propose a flexilbe antenna module to be integrated into an active electronically scanning array (AESA) with controlled sidelobe level over a wide angular range, exhibiting polarization reconfigurability with low cross-polarization level and high isolation. For this purpose, analytical and numerically efficient techniques for the synthesis of the aperture distribution and the correct evaluation of the radiating features (e.g., beamwidth, pointing angle, sidelobe levels, etc.) are presented in order to grant a real-time control of the digital beamforming network. A sub-array module demonstrator is fabricated and measured to corroborate the concept.

Keywords: phased arrays; planar arrays; antenna radiation patterns; beam steering; radar antennas; radar applications

---

1. Introduction

In the last few years, the attention on software-defined radar (SDR) has grown exponentially. As a matter of fact, this approach offers a series of advantages that goes from digital beamforming to hardware flexibility [1]. The possibility to drive an active electronically scanning array (AESA) with an SDR platform would pave the way for a fully-digital radiofrequency (RF) front-end with unprecedented capabilities in terms of reconfigurability, re-use of hardware, and modularity. In the past, the growth in SDR platforms has been limited mostly by the low-speed interface and the low sampling frequency of the analog-to-digital converters (ADC) and digital-to-analog converters (DAC) [2,3]. However, the recent developments in the state of the art for DAC–ADC components allowed for developing *fully digital* L-band products, and nowadays fully digital X-band architectures represent the next step on the SDR framework [4,5].

Recently, SDR platforms have been configured and tested to drive passive bistatic radar (PBR) systems based on linear arrays to perform detection and tracking functions. However, these works [6–9] were mainly focused on the software implementation of the calibration network and of the Digital Signal Processing (DSP) architecture, whereas the software implementation of a fully digital beamformer was not analyzed in detail. Moreover, in order to fully exploit the potentialities of the SDR approach, the design flexibility has to be ensured at the hardware level. Antenna elements that allow for dynamic polarization and beam steering are thus required, especially when used in large planar AESA to reach the high-gain and high-coverage requirements of radar tracking systems.

To this aim, we discuss here the design of a 40 × 40 planar AESA capable of scanning a very directive beam over a wide angular range with controlled sidelobe in C band. Efficient analytical and numerical methods for both the realization of a Tseng–Cheng beamforming network [10] and the evaluation of the main radiating properties are proposed to easily interface the AESA with an SDR platform. In order to respond to the needs of design flexibility and high performance, inspired by the recent works on multifunction phased array radar (MPAR) [11–13], we propose an attractive unit cell fed with two ports that can be independently controlled in amplitude and phase, and capable of providing low cross-polarization and high isolation. In order to corroborate the antenna performance, a 4 × 6 array demonstrator is fabricated and measured, showing good agreement with the expected theoretical results.

The paper is organized as follows. In Section 2 we describe the targeted antenna performance of the AESA and present analytical methods for both the design of the digital beamformer and the evaluation of the AESA radiating features. In Section 3 the antenna element is described and designed to ensure polarization flexibility, low cross-polarization, and high isolation. In Section 4 the fabrication and experimental validation of a 4 × 6 demonstrator is shown. Finally, conclusions are drawn in Section V.

2. Array Design

We aim at designing a planar AESA capable of producing a pencil beam (about 3° of half-power beamwidth (HPBW), at broadside) over an angular range of 60° on the elevation plane and a full coverage on the azimuthal plane with a sidelobe level (SLL) of -30 dB to be maintained for the whole scanning range and over the design frequency range, also exhibiting polarization reconfigurability with a low cross-polarization level and high isolation. C band is considered for the design, with a bandwidth of 10%. The main frequencies in the design band will be called f_{min} for the lower frequency, f_{max} for the higher frequency and f_0 for the central frequency. In particular, $f_{\mathrm{min}} = 0.95 f_0$ and $f_{\mathrm{max}} = 1.05 f_0$. The latter properties can be demanded to the element factor and will be discussed in Section III. In the next subsections, we focus on the design of the Array Factor (AF) with analytical techniques to meet the constraints of having a pencil beam with controlled SLL over the entire scanning range.

2.1. Analytical Techniques

2.1.1. Sidelobe Level

We first examine the abovementioned specifications to find the most suitable technique for the realization of an efficient digital beamformer. The requirement of an invariant SLL considerably restricts the available beamforming techniques. As a matter of fact, apart from optimization algorithms (see, e.g., the excellent reviews in [14,15] and refs. therein), only the Tseng–Cheng technique [10] guarantees a constant SLL at arbitrary azimuthal cuts and for any scan angle. Moreover, the Tseng–Cheng technique has the following advantages compared to other techniques: *i)* it is fully analytical, *ii)* it is computed once, without requiring to refresh the amplitude coefficients as the scan angle is changing, *iii)* being based on the Dolph–Chebyshev technique, it provides the minimum beamwidth for a given SLL [10]. All these aspects make the Tseng–Cheng technique particularly attractive for its implementation in an SDR-driven beamforming network.

In order to implement the Tseng–Cheng technique we assume an even number of elements along the two main directions, i.e., $N_x = N_y = M = 2N$ and quadrantal symmetry of the amplitude coefficients, i.e., $a_{mn} = a_{-m,n} = a_{m,-n} = a_{-m,-n}$ (the extension to rectangular lattices has been proposed in [16]). Under this hypothesis the AF can conveniently be recast as [10,17]:

$$\mathrm{AF}(\theta, \phi) = 4 \sum_{m=1}^{N} \sum_{n=1}^{N} a_{mn} \cos[(2m-1)u] \cos[(2n-1)v] \tag{1}$$

where $u = 0.5kd_x(\sin\theta\cos\phi - \sin\theta_0\cos\phi_0)$ and $v = 0.5kd_y(\sin\theta\sin\phi - \sin\theta_0\sin\phi_0)$, $d_x(d_y)$ are the spacing along the $x(y)$-axis, θ and ϕ are the elevation and azimuthal angles of the spherical coordinate system, $k = 2\pi/\lambda$ is the free-space wavenumber, λ being the free-space wavelength. As shown in [10], an invariant SLL over the entire angular range can be achieved if the amplitude coefficients are set equal to

$$a_{mn} = \frac{1}{N^2}\sum_{p=1}^{N}\sum_{q=1}^{N} T_{M-1}\left[w_0\cos\frac{\pi(p-\frac{1}{2})}{2N}\cos\frac{\pi(q-\frac{1}{2})}{2N}\right] \cos\left(\frac{\pi(m-\frac{1}{2})(p-\frac{1}{2})}{N}\right)\cos\left(\frac{\pi(n-\frac{1}{2})(q-\frac{1}{2})}{N}\right) \tag{2}$$

where $T_{M-1}[\cdot]$ is the Chebyshev polynomial of the first kind and order $M-1$, w_0 is related to the SLL through the expression $w_0 = \cosh[1/(M-1)\text{arccosh}(\text{PSR})]$, where PSR is the peak-to-sidelobe ratio, i.e., $\text{PSR} = \sqrt{1/\text{SLL}}$ (assuming all quantities in linear scale). In order to avoid grating lobes the usual condition for untapered distributions modifies as follows:

$$\frac{d_{x(y)}}{\lambda} < \frac{1 - [\arccos(1/w_0)]/\pi}{1 + \sin\theta_{\max}} \tag{3}$$

where $\theta_{\max}$ is the maximum scan angle. As is clear from the expression (2), its straight implementation would require four nested loops to evaluate all the coefficients (viz., two for the m and n elements indices, and two for the p and q summation indices), thus resulting time-consuming computations. To take advantage of the MATLAB potentialities in handling matrix calculations, it is therefore important to recast (2) to avoid as much as possible the use of nested loops. Indeed, the two summations in (2) can conveniently be expressed as a quadratic form:

$$a_{mn} = N^{-2}\underline{t}_p(m)\underline{\underline{T}}_{pq}\underline{t}_q(n) \tag{4}$$

where $\underline{t}_p(m) = \cos[\pi(m-0.5)(\underline{p}-0.5)]/N$, $\underline{t}_q(n) = \cos[\pi(n-0.5)(\underline{q}-0.5)]/N$, and $\underline{\underline{T}}_{pq} = T_{2N-1}\{w_0\cos[\pi(p-0.5)/2N]\cos[\pi(q-0.5)/2N]\}$ with $\underline{p} = 1,2\ldots N$ and $\underline{q} = 1,2\ldots N$ row and column vectors of N elements, respectively.

2.1.2. Beamwidth

As is known, the HPBW ($\Theta_{x(y)0}$) at broadside along the principal planes of a uniform planar array is well approximated by the formula:

$$\Theta_{x(y)0} = \pi - 2\arccos\left(\frac{0.886\lambda}{2N_{x(y)}d_{x(y)}}\right) \simeq \frac{0.886\lambda}{N_{x(y)}d_{x(y)}} \tag{5}$$

where the last approximation is obtained in the limit of large arrays (we recall that $\arccos(x) \simeq \pi/2 - x$ for $x \to 0$).

As the beam is scanned at a generic angle (θ_0, ϕ_0), the beamwidth over the two principal planes changes according to the following equations [18]

$$\Theta_{\text{h}} = \left(\sqrt{\cos^2\theta_0[\Theta_{x0}^{-2}\cos^2\phi_0 + \Theta_{y0}^{-2}\sin^2\theta_0,\phi_0]}\right)^{-1} \tag{6}$$

$$\Psi_{\text{h}} = \left(\sqrt{\Theta_{x0}^{-2}\sin^2\phi_0 + \Theta_{y0}^{-2}\cos^2\phi_0}\right)^{-1} \tag{7}$$

where Θ_{h} and Ψ_{h} represent the HPBW on the elevation plane, and its orthogonal plane, respectively. When the array has the same number of elements and the same spacing over the x and y axes (as in the case shown discussed here), $\Theta_{x0} = \Theta_{y0} = \Theta_{0\text{h}}$, thus $\Psi_{\text{h}} = \Theta_{0\text{h}}$ is constant, whereas $\Theta_{\text{h}} = \Theta_{0\text{h}}\sec\theta_0$,

doi:10.20944/preprints202405.1892.v1

giving rise to an unavoidable pattern distortion in the scanning towards endfire (viz., for $\theta_0 = 60^\circ$, $\sec\theta_0 = 2$, hence Θ_h is doubled). While the numerical evaluation of the beamwidth along the plane $\phi = \phi_0$ is quite straightforward, a few words should be spent on the evaluation along the orthogonal plane. Indeed, the AF is represented as a function of θ and ϕ, hence the HPBW over the ϕ_0-plane is simply given by the distance between the -3 dB points along θ, while the HPBW over the orthogonal plane needs an explicit definition of the angle ψ. This definition can be recovered from simple geometrical considerations and leads to the following expression

$$\psi = \arcsin[\sin\tilde{\theta}\sin(\tilde{\phi} - \phi_0)] \tag{8}$$

where $\tilde{\theta}$ and $\tilde{\phi}$ are the zeros of the equation $\tan\theta\cot\theta_0 = \sec(\phi - \phi_0)$, that is but the equation of the plane orthogonal to the unit vector $\hat{\theta}$ in (θ_0, ϕ_0), i.e., the plane defined by $\hat{r} \cdot \hat{\theta}|_{\theta_0,\phi_0} = 0$, where $\hat{r}$ is the position unit vector. We should note that $\tilde{\theta}$ and $\tilde{\phi}$ should be sought by means of a root-finding algorithm. Once all the $\tilde{\theta}$, $\tilde{\phi}$ pairs are found, the AF calculated at $(\tilde{\theta}, \tilde{\phi})$ must be rearranged according to the ordering given by $-\pi/2 \leq \psi(\tilde{\theta}, \tilde{\phi}) \leq \pi/2$. Then, the -3 dB points along ψ can finally be found.

However, when tapering techniques for SLL reduction are taken, the HPBWs are notably affected and accounted for by the *spreading factor* s_f. In particular, if one applies a Dolph–Chebyshev technique (as that of Tseng–Cheng) to achieve an SLL of -30 dB, the s_f is given by

$$s_\mathrm{f} = 1 + 0.636\left\{\frac{2}{\mathrm{PSR}}\cosh\left[\sqrt{(\operatorname{arccosh}\mathrm{PSR})^2 - \pi^2}\right]\right\}^2. \tag{9}$$

Therefore, Θ_{x0} and Θ_{y0} as they appear in (5) have to be multiplied by s_f as given by (9).

2.1.3. Bandwidth

As is well known from array theory [17,19], the array bandwidth is severely limited by the phase shifters unless one resorts to true time-delay devices. The latter usually require expensive and complex architectures that can only be justified when the array needs to guarantee an excellent performance over a considerably large bandwidth. Conversely, for relatively small fractional bandwiths as those considered here, phase shifters are usually preferred. As a result, the beam is exactly steered at a point in space (θ_0, ϕ_0), only at the center frequency f_0, i.e., when the u and v terms appearing in (1) are evaluated at $k_0 = k(f_0)$. As a result, for $f \neq f_0$, the beam is *squinted* by an angular deviation $\Delta\theta$ from the theoretical pointing angle θ_0 given by the formula

$$\Delta\theta = |\arcsin(\sin\theta_0 f_0/f) - \theta_0|. \tag{10}$$

The main consequence of the beam squint is that the -3 dB fractional bandwidth $\Delta f/f_0$ is affected. In particular, for a linear array of length L it is determined by the expression [19]

$$\frac{\Delta f}{f_0} = 0.886 s_\mathrm{f}\frac{\lambda_0}{L\sin\theta_0} \simeq s_\mathrm{f}\Theta_{0\mathrm{h}}\csc\theta_0 \tag{11}$$

λ_0 being the center wavelength. Again, the last expression is obtained in the limit of large arrays using the right-hand side of (5).

2.2. Numerical Results

The analytical techniques presented in the previous paragraphs are exploited here in a proof-of-concept to test their effectiveness and accuracy in the array synthesis and its performance evaluation.

The proof-of-concept is chosen to fit the constraints mentioned at the beginning of Section 2, namely SLL < -30 dB, $\theta_{0,\max} = 60^\circ$, $\Theta_{0\mathrm{h}} = 3^\circ$ over the $f_\mathrm{min} - f_\mathrm{max}$ range. In order to fulfill the SLL requirement, we have to accept a spreading factor of about 1.3, but only a slight modification to the condition for avoiding grating lobes ($w_0 \simeq 1.0057$). We thus set $d_x = d_y = \lambda_0/2$ which mostly satisfies

(3). With these numbers at hand, it is found from (5) that $N_x = N_y = 40$ provides for $\Theta_{0\text{h}}$ around 2.5° that, after taking into account the spreading factor (viz., $s_{\text{f}} \simeq 1.3$), yields 3.3°. Under this condition the -3 dB fractional bandwidth at the maximum scan angle would be around 6.6%. Using (11), it is found that the targeted bandwidth performance would be reached by either limiting the maximum scan angle to 40°, or broadening the broadside beamwidth to about 4.5°. In the following we consider the original setting, thus accepting a reduction in the operating bandwidth.

Therefore, we consider a 40×40 planar array with $d/\lambda = 0.5$ spacing among the elements and apply the Tseng–Cheng technique to obtain an invariant SLL of -30 dB. The distribution of the amplitude coefficients is reported in Figure 1. As shown, the coefficients at the four corners are almost zero, thus the corresponding elements may not be fed, with minor impact on the radiating performance. In particular, in Figure 2(a)–(d) a comparison is shown between the normalized power radiation patterns produced with an *ideal* (i.e., keeping all the coefficients) Tseng–Cheng distribution (see Figure 2(a)), and those produced by setting to 0 the coefficients below 0.01 (see Figure 2(b)), 0.05 (see Figure 2(c)), and 0.1 (see Figure 2(d)), when the array is scanned at ($\theta_0 = 60°$, $\phi_0 = 45°$). For a threshold of 0.01 no appreciable difference is seen with the ideal case, but in the former case one would achieve a reduced filling factor of 83%. As the threshold raises, the filling factor reduces further (viz., 62% and 43% for thresholds of 0.05 and 0.1, respectively), but the SLL raises as well (viz., peaks of -26 dB and -21 dB for thresholds of 0.05 and 0.01, respectively). As a result, further reductions of the number of elements should not be considered as this would require optimization techniques for sparse arrays, an aspect that goes beyond the scope of this work.

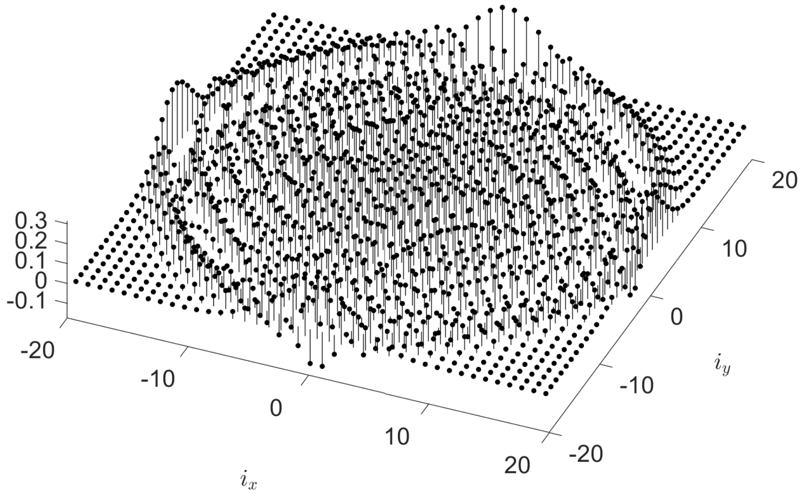

Figure 1. Map of the amplitude coefficients of a 40×40 array for the design specifications on the beam given in the text through the Tseng–Cheng technique.

doi:10.20944/preprints202405.1892.v1

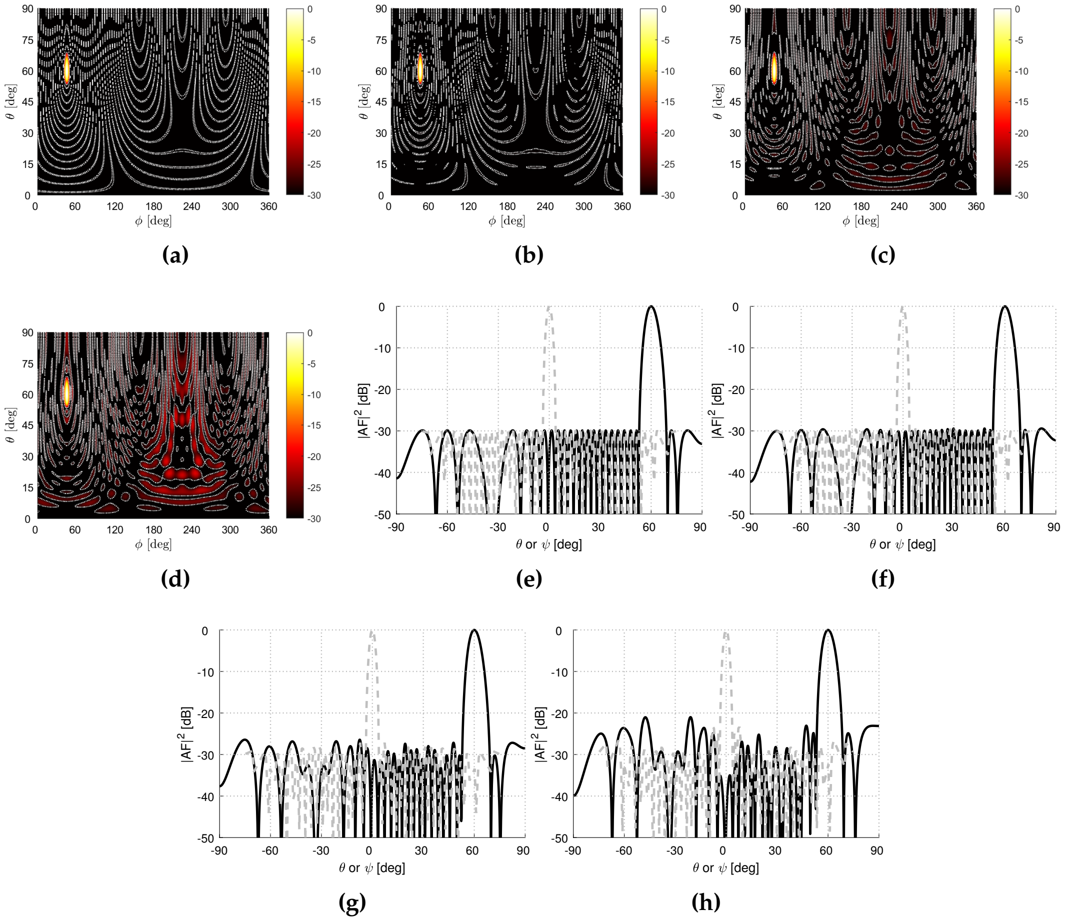

(a) (b) (c) (d) (e) (f) (g) (h)

Figure 2. Color maps of $|\mathrm{AF}|^2/|\mathrm{AF}|^2_{\mathrm{max}}$ vs. θ and ϕ, for (a) an ideal Tseng–Cheng technique, (b)–(d) a Tseng–Cheng technique neglecting coefficients with amplitudes below 0.01, 0.05, and 0.1, respectively, when $\theta_0 = 60^\circ$, $\phi_0 = 45^\circ$. The dotted-dashed lines represent the -30 dB iso-lines of the contour plot. Parameters of the Tseng–Cheng technique and of the array are reported in the text. (e)–(h) The radiated power density normalized to the absolute maximum (i.e., $|\mathrm{AF}|^2/|\mathrm{AF}|^2_{\mathrm{max}}$) along the principal planes (in black solid lines and dashed gray lines, the plane $\phi = \phi_0$, and the orthogonal one, respectively), for the same cases analyzed in (a)–(d), respectively.

The effect of the elements reduction is even more appreciable looking at the 1-D normalized power patterns along the two principal planes (solid black and gray dashed lines in Figure 2(e)–(h)). It is noted that the patterns along the elevation plane are more affected than those along the orthogonal plane in all cases. Interestingly, the beamwidths are not affected by the elements reduction, and their numerical evaluation agree well (a percent error less than 10%) with the formulas provided in (5)–(7).

With respect to the bandwidth performance, the beam squint $\Delta\theta$ and the gain loss are evaluated as a function of the frequency in Figure 3(a), (b). It is seen that the numerical evaluation of the beam squint (solid black line in Figure 3(a)) compares well with the theoretical prediction of (10) (dashed grey line in Figure 3(a)), and reveals a beam squint of about 3° within the -3 dB bandwidth shown in Figure 3(b). The beamwidths along the principal planes and as a function of frequency are also shown in Figure 4 where their numerical evaluation is compared against the analytical expressions provided in Eqs. (6)–(7) accounting for the spreading factor. As commented before, the agreement is good, showing a percent error lower than 10% which remains rather constant with respect to the frequency. Interestingly, it is noted that Ψ_{h} is considerably less affected by the frequency with respect to Θ_{h}.

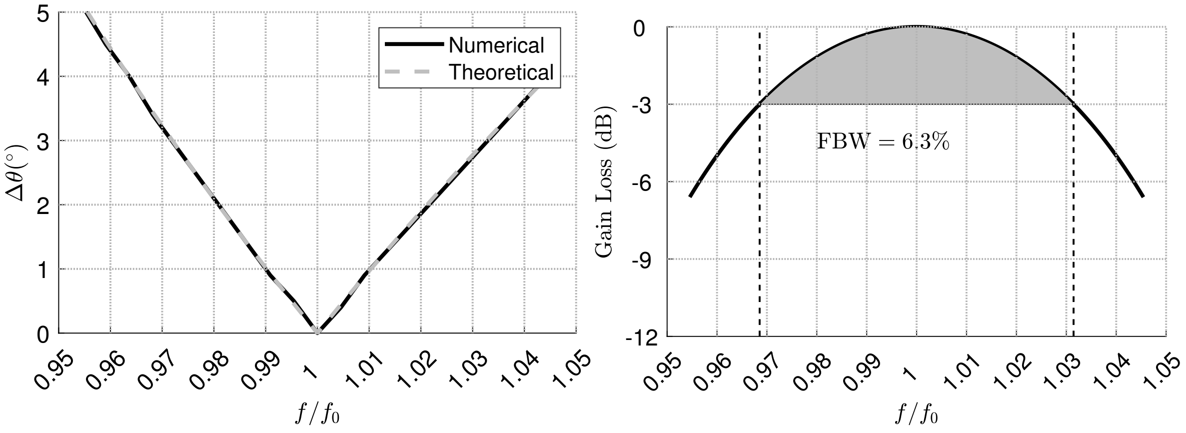

(a) **(b)**

Figure 3. (a) Beam squint $\Delta\theta$ and (b) gain loss vs. f in the range $f_{\text{min}} = 0.95 f_0$, $f_{\text{max}} = 1.05 f_0$. In (a) numerical (theoretical) results are reported with solid black (dashed grey) lines.

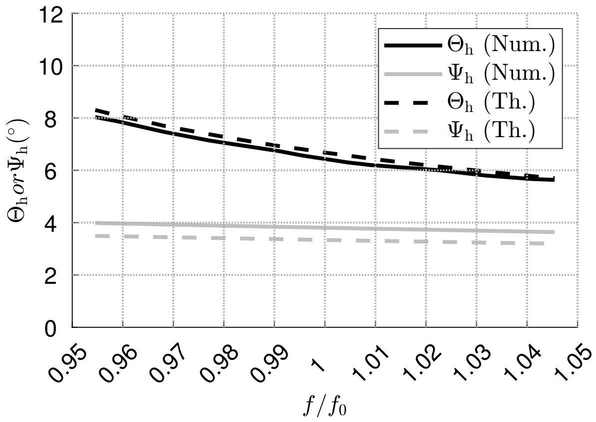

Figure 4. The beamwidths along the principal planes Θ_h (in black) and Ψ_h (in grey) vs. f in the range $f_{\text{min}} - f_{max}$. Numerical (theoretical) results are reported with solid (dashed) lines.

3. Element Design

3.1. Antenna Structure

In the previous Section 2, the array has been designed to obtain a radiation pattern featuring a pencil beam with a HPBW of about 3° and a SLL lower than −30 dB to be scanned over an angular range of 60° on the elevation plane and 360° on the azimuthal plane. At this stage, it is necessary to design the antenna element to meet the requirements of low cross-polarization and isolation over the $f_{\text{min}} - f_{\text{max}}$ band, and ensure polarization reconfigurability. In this regard, the low cross-polarization requirement calls for elements that are symmetric along the principal planes, such as square patch antennas [18]. The latter, however, rarely maintain such performance over fractional bandwidths as large as 10%, unless stacked configurations (typically with the top substrate thicker than the bottom one) are considered [20,21]. As per the polarization reconfigurability, two ports are considered and fed with aperture-coupled techniques to guarantee the required isolation [11,22]. These aspects have led to consider the antenna architecture proposed in [11] as a reference structure to be suitably modified and optimized to meet our requirements in the $f_{\text{min}} - f_{\text{max}}$ band.

3.2. Full-Wave Results

The aforementioned antenna, that is shown in Figure 5 (a), consists of a *dual-pol aperture-coupled stacked patch* made of three dielectric substrates. On the bottom of the lower substrate (Rogers Kappa438) two printed microstrip lines are used to excite two slots on the top of the same substrate. The plane where the slots are located is also used as a ground plane. On the lower part of the upper substrate there is a parasite patch slightly smaller than the main patch printed on the top of the same layer. Both upper and middle dielectric layers are realized with a Taconic TLX-8 laminate.

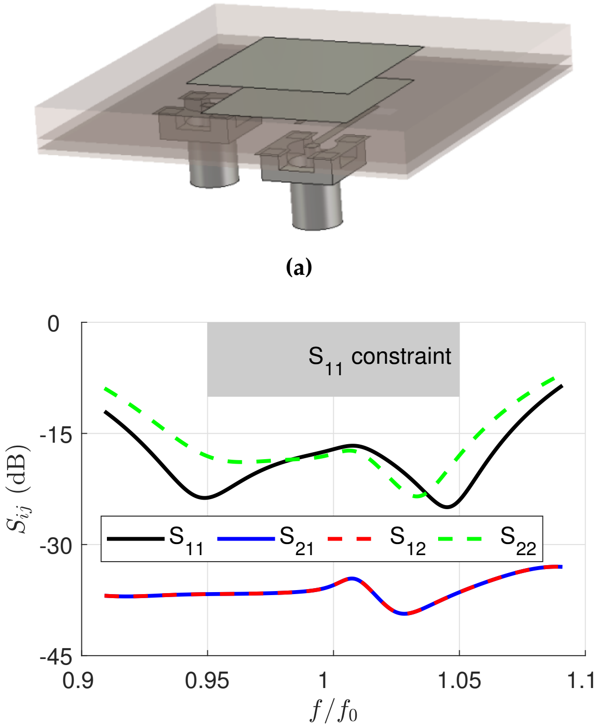

(a)

(b)

Figure 5. (a) Proposed antenna, (b) S parameters of the optimized radiating element.

The radiating element has been simulated in CST [23] in a 2-D periodic environment, in order to take into account the coupling effects that occur in a 2-D array. The S-parameters results obtained from the simulation of the optimized antenna are shown in Figure 5 (b). The isolation between ports is rather satisfactory, with values below -30 dB, as well as the reflection coefficient that is well below -10 dB in the frequency range of interest.

In Figure 6 the radiation patterns are shown on the principal planes, and as expected from the reflection coefficients a low cross polarization level and a symmetric co-polar pattern is obtained for both the H- and V-port excitations. To complete the picture, full-wave 3-D radiation patterns for co-polar and cross-polar components of both H and V port are shown in Figure 7. A detailed view of the resulting antenna is also shown in Figure 8, whereas in Table 1 a list of the various design parameters is reported.

Table 1. Design parameters for the radiating element

Substrates/Patch/Connectors		Slots		Strips	
Parameter	Value [mm]	Parameter	Value [mm]	Parameter	Value [mm]
p	26.98	$d_{x\mathrm{Hslot}}$	12.42	$d_{x\mathrm{Hstrip}}$	4.80
h_1	0.51	$d_{y\mathrm{Hslot}}$	10.00	$d_{y\mathrm{Hstrip}}$	13.05
h_2	0.79	$d_{x\mathrm{Vslot}}$	6.02	$d_{x\mathrm{Vstrip}}$	8.55
h_3	2.36	$d_{y\mathrm{Vslot}}$	12.56	$d_{y\mathrm{Vstrip}}$	4.80
w_{p1}	12.9	w_{Hslot}	1.84	w_{Hstrip}	0.9
h_{p1}	12.9	h_{Hslot}	1.84	l_{Hstrip}	8.87
w_{p2}	14.5	w_{Hslit}	0.26	w_{Tstrip}	0.55
h_{p2}	14.5	l_{Hslit}	3.29	l_{Tstrip}	6.00
$d_{x\mathrm{H}}$	5.50	w_{Vslot}	1.85	w_{Vstrip}	0.90
$d_{y\mathrm{H}}$	13.49	h_{Vslot}	1.85	l_{Vstrip}	11.37
$d_{x\mathrm{V}}$	9.00	w_{Vslit}	0.15	—	—
$d_{y\mathrm{V}}$	5.50	l_{Vslit}	2.25	—	—

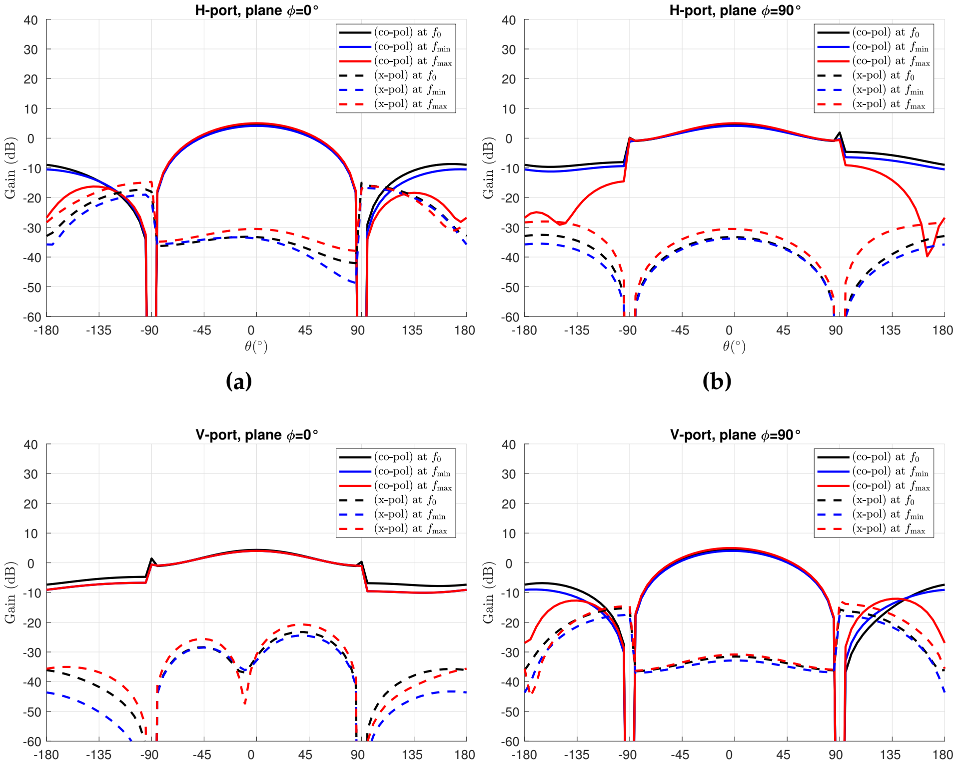

(a)

(b)

(c)

(d)

Figure 6. (a)–(d) Main cuts of the radiation pattern for the optimized radiating element. (a)–(b) refer to H-port excitation; (c)–(d) refer to V-port excitation. (a) and (c) show the $\phi = 0°$ cuts, whereas (b) and (d) show the $\phi = 90°$ cuts.

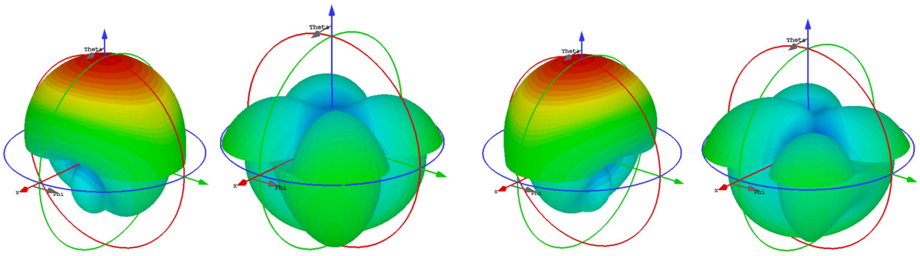

(a) **(b)** **(c)** **(d)**

Figure 7. (a)-(d) Radiation patterns for (a)–(b) horizontal polarization, (c)–(d) vertical polarization at f_0. In (a)-(c) co-polar component, in (b)–(d) cross-polar component.

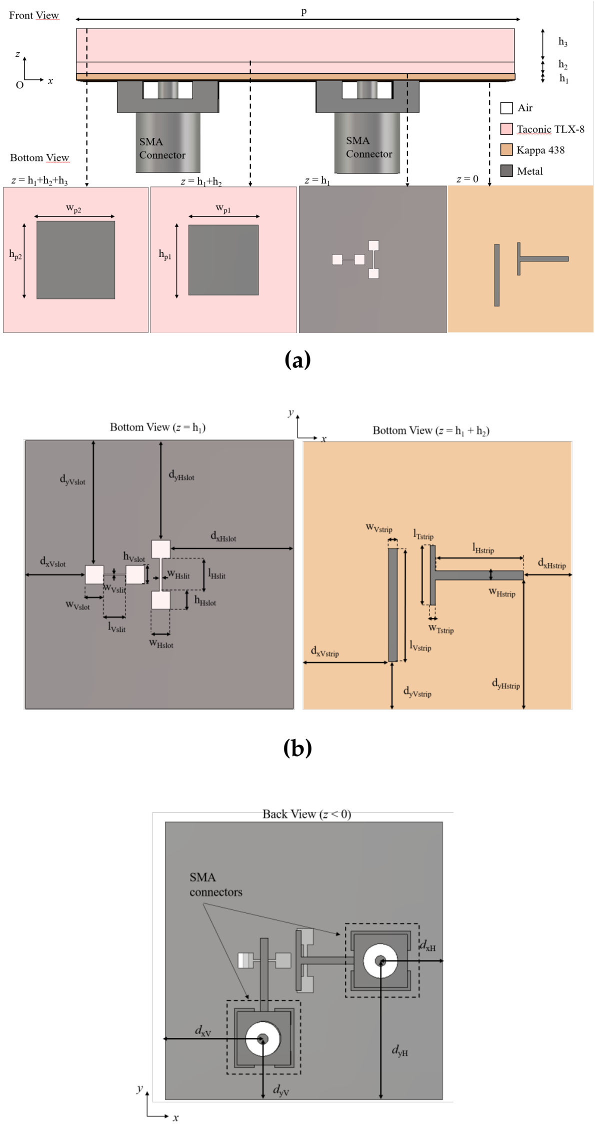

(a)

(b)

(c)

Figure 8. (a)–(c) Detailed antenna structure. (a) Front view and cross sections at different heights. (b) Back view from the ground plane and feeding structure. (c) Back view from SMA connectors.

4. Sub-Array Demonstrator

4.1. Full-Wave Results

The radiating element analyzed in the previous Section is here used on a 2 × 8 array to realize a demonstrator. This analysis is particularly useful to understand if the unit-cell simulation results (that emulate an infinite array environment) are consistent with a finite array simulation setup.

In Figure 9, the F-parameters obtained from the 2 × 8 array simulation are shown. F-parameters are used to calculate antenna coupling coefficients sources in the case of simultaneous excitation, when is not possible to apply the general S-Parameter definition anymore, and can be therefore considered as active scattering parameters. In particular, $F_{\mathrm{hh(vv)}}$ parameters refers to the reflection coefficient of a port V(H) when all the other ports H(V) are excited, while the $F_{\mathrm{hv(vh)}}$ parameters refers to the isolation between the ports H(V) when all the others V(H) are excited. In particular, in the $f_{\mathrm{min}} - f_{\mathrm{max}}$ band F_{hh} and F_{vv} parameters are well below -10 dB, and have a similar behavior to the reflection coefficients obtained from the unit cell simulation for both H and V ports. The same holds for the F_{hv} and F_{vh} parameters, that are similar to the transmission coefficients values obtained from the unit-cell simulation. The good agreement between the F parameters of the array simulation with the S parameters of the unit-cell simulation demonstrate that the latter takes into account very well the mutual coupling effects.

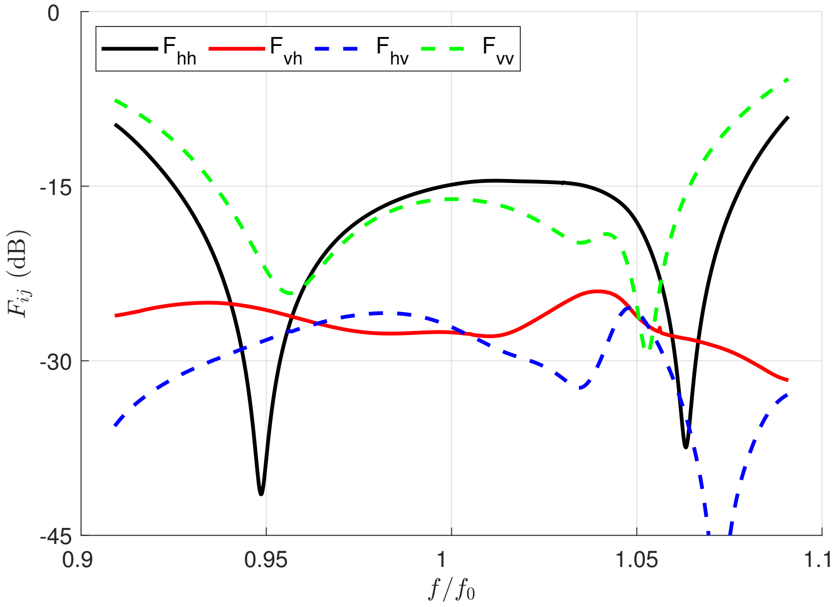

Figure 9. 2x8 array F parameters of the optimized radiating element.

Moreover, in Figure 10 and Figure 11 are shown the 1-D and 3-D far-field radiation patterns, respectively. It can be noticed that the radiation pattern of the array is squeezed along the array axis due to the array factor. On the transverse axis, the total pattern remains almost unaffected with respect to the element pattern provided by the unit-cell. In all cases, the cross-polar values remain mostly below -20 dB, as expected from the F parameters.

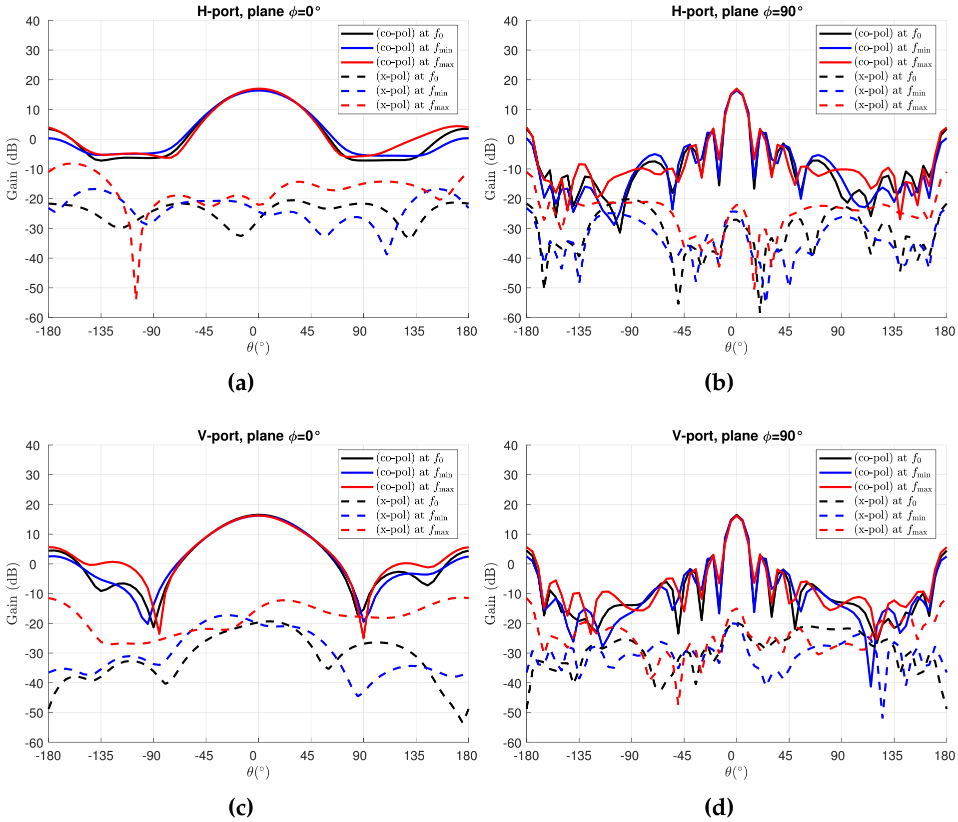

(a) **(b)**

(c) **(d)**

Figure 10. (a)-(d) Main cut of the radiation patterns for the 2x8 array. (a)-(b) show results while the H port is excited, (c)-(d) while the V port is excited. In (a)-(c) the $\phi = 0°$ cut, in (b)-(d) the $\phi = 90°$ cut is plotted.

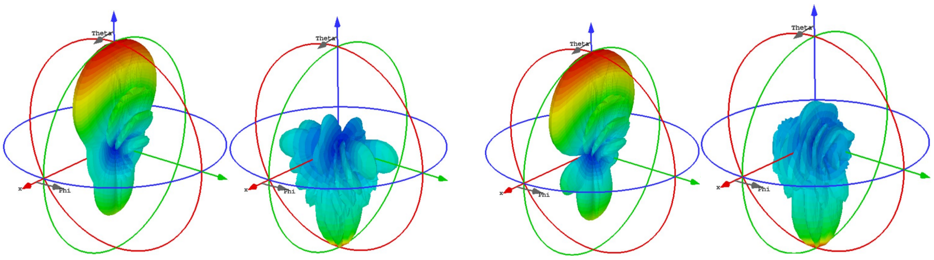

(a) **(b)** **(c)** **(d)**

Figure 11. (a)-(d) Radiation patterns for (a)-(b) horizontal polarization, (c)-(d) vertical polarization at f_0. In (a)-(c) co-polar component, in (b)-(d) cross-polar component.

4.2. Experimental Results

Two prototypes of this 2×8 array have been fabricated and have been used to implement a total 4×8 array for the measurement setup. The prototypes are placed on a metallic plane properly shaped, and two plexiglass bars are used to secure the two prototypes on the metallic support. For that reason, two columns of radiating elements are unavailable, and the array under test is a 4×6. The measurement setup is shown in Figure 12 (a), with all the measurements performed in an anechoic chamber.

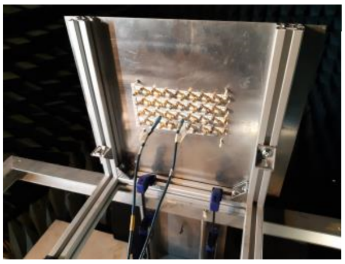

(a)

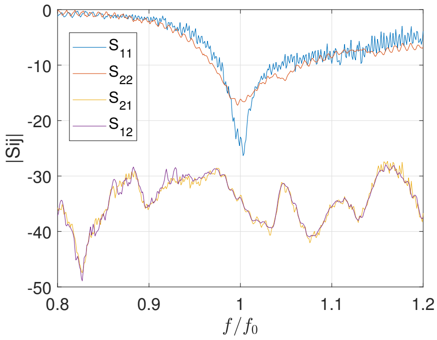

(b)

Figure 12. (a) Array demonstrator, (b) Measured S Parameters.

The measured S_{ij} parameters are shown in Figure12 (b) for both V and H port, respectively signed as port 1 and port 2. The measurements show a frequency shift of the resonance, that is centered to $\tilde{f_0} = f_0 - 0.09f_0$ instead of f_0. However, a fractional bandwidth of 10% is achieved between $\tilde{f}_{\text{min}} = f_{\text{min}}$ - $0.09f_0$ and $\tilde{f}_{\text{max}} = f_{\text{max}}$ - $0.09f_0$, and the isolation between ports is lower than -30 dB. The frequency shift can be attributed to different aspects:

1. An important PCB curvature has been observed. This is due to the manufacturing process, and at the design frequency this issue can affect the antenna gain and the S_{ij} parameters;
2. Possible variations of the dielectric constant respect to the one shown in the data-sheet of the materials;
3. Possible interactions between the metallic support and the radiating elements. These metallic parts are very near to the radiating board, and their effect could be not negligible.

With this setup, it is possible to evaluate the total pattern, from the active reflection coefficient. As is known, the total pattern can be obtained by pattern multiplication between the array factor and the active element pattern $G_{\text{e,act}}$, which is in turn related to the active reflection coefficient Γ_{act} for every scan angle θ_0, ϕ_0 through the relation [24]

$$G_{\text{e,act}}(u_0, v_0) = \frac{4\pi \cos\theta_0 p_x p_y}{\lambda^2}(1 - |\Gamma_{\text{act}}(u_0, v_0)|^2) \tag{12}$$

where p_x and p_y represent the periodicity of the array along the x- and y-axis, respectively, with $u_0 = \sin\theta_0 \cos\phi_0$ and $v_0 = \sin\theta_0 \sin\phi_0$.

The results obtained with (12) from the measurement of the scattering parameters are shown in Figure 13, whereas in Figure14 are shown the principal planes of the active element pattern for both polarizations, and the gain plot versus frequency at broadside for both polarizations. From these results it can be seen that the active element gain has a quite flat and regular shape in the uv plane and a peak value near to the theoretical expected value in the $\tilde{f}_{\text{min}} - \tilde{f}_{\text{max}}$ band. The main reason for this behavior is due to the frequency shift reported in Figure 12 (b) and in Figure 14, where the peak gain and the minimum of the reflection coefficient are located around $\tilde{f_0}$.

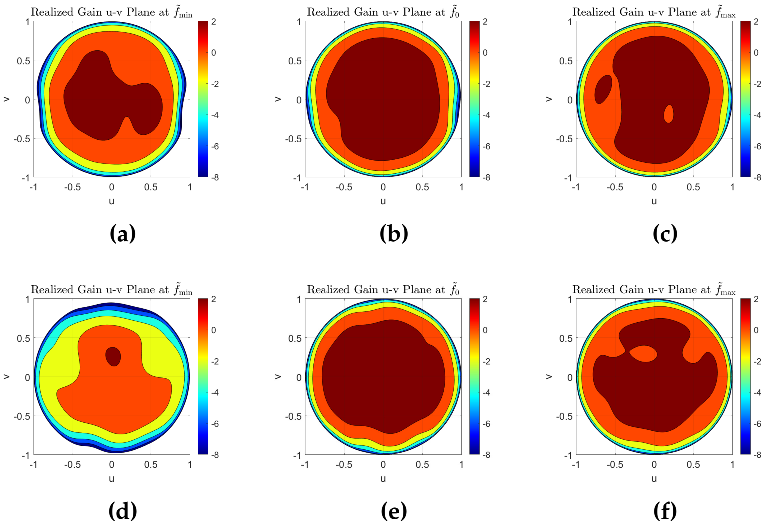

(a) (b) (c)

(d) (e) (f)

Figure 13. (a)-(c) Gain measurements on the uv plane for H polarization at (a) $\tilde{f}_{\min}$, (b) $\tilde{f}_0$, (c) $\tilde{f}_{\max}$. (d)–(f) As in (a)–(c) but for V polarization.

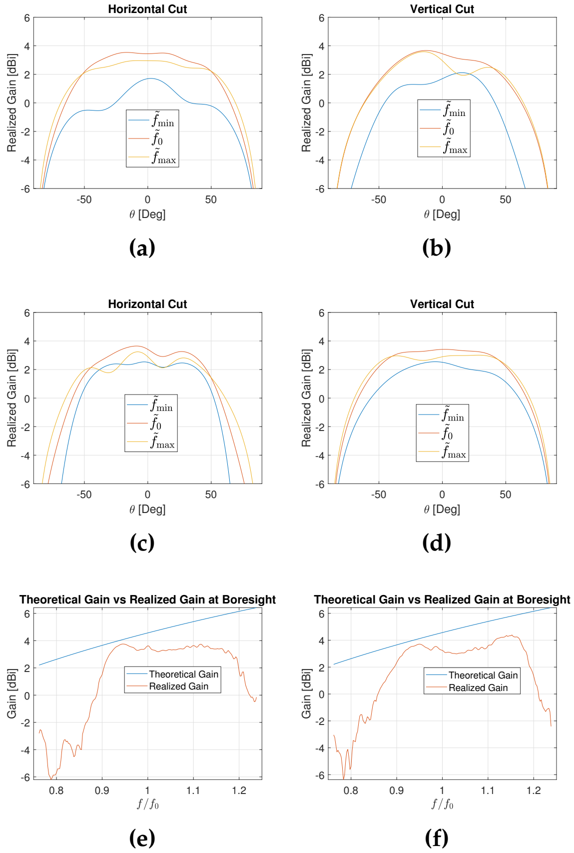

(a) (b)

(c) (d)

(e) (f)

Figure 14. Gain obtained from the Γ_{act} measurements for the three main frequencies ($\tilde{f}_{\min}$, $\tilde{f}_0$, $\tilde{f}_{\max}$) on the plane (a) $\phi = 0^\circ$ and (b) $\phi = 90^\circ$ for H polarization. In (c) and (d), as in (a) and (b) but for V polarization. In (e) and (f) it is shown the gain in dB obtained from Γ_{act} measurements for $\theta = 0^\circ$ versus the expected gain, respectively for H and V polarization

5. Conclusions

A planar AESA capable of producing a pencil beam with invariant sidelobe level over a wide angular range and at any frequency in C band has been designed with fully analytical techniques. An efficient MATLAB implementation of the Tseng–Cheng technique is presented that looks particularly attractive for realizing a Software-Defined-Radar (SDR) interface for the real-time control of the beamforming network. The radiating performance of a case study is analyzed in detail showing the effects of a reduction of the filling factor. A smaller 4 × 6 demonstrator has been fabricated and measured to test the main radiating performance of the proposed antenna architecture. The flexibility of the polarization control, the low level of cross-polarization, and the good isolation between ports over a 10% fractional bandwidth make this prototype attractive for future SDR applications.

Acknowledgments: This work has been developed under the contract $\mathrm{COLB}-\mathrm{CTR}-2017-009-\mathrm{A}$ between Leonardo S.p.A. and Sapienza University of Rome.

References

1. Fulton, C.; Yeary, M.; Thompson, D.; Lake, J.; Mitchell, A. Digital Phased Arrays: Challenges and Opportunities. *Proc. IEEE* **2016**, *104*, 487–503. doi:10.1109/JPROC.2015.2501804.
2. Kwag, Y.K.; Jung, J.S.; Woo, I.S.; Park, M.S. Modern software defined radar (SDR) technology and its trends. *J. Electromagn. Eng. Sci.* **2014**, *14*, 321–328.
3. Debatty, T. Software defined radar a state of the art. 2nd International Workshop on Cognitive Information Processing (CIP); , 2010; pp. 253–257.
4. Ciociola, A.; Infante, L.; Ricciardella, N.; Solimene, R.; Felaco, M.; Pellegrini, G. Digitally Synthesized Antenna Test Bench for Next Generation Phased Array Systems. IEEE Int. Conf. Phased Array Syst. Technol., 2022, pp. 1–6. doi:10.1109/PAST49659.2022.9975028.
5. Castillo-Rubio, C.F.; Pascual, J.M. Current Full Digital Phased-Array Radar developments for Naval applications. IEEE Int. Conf. Phased Array Syst. Technol., 2019, pp. 1–6. doi:10.1109/PAST43306.2019.9021011.
6. Capria, A.; Petri, D.; Moscardini, C.; Conti, M.; Forti, A.C.; Massini, R.; Cerretelli, M.; Ledda, S.; Tesi, V.; Dalle Mese, E.; others. Software-defined Multiband Array Passive Radar (SMARP) demonstrator: A test and evaluation perspective. OCEANS 2015; IEEE, , 2015; pp. 1–6.
7. Capria, A.; Giusti, E.; Moscardini, C.; Conti, M.; Petri, D.; Martorella, M.; Berizzi, F. Multifunction imaging passive radar for harbour protection and navigation safety. *IEEE Aerosp. Electron. Syst. Mag.* **2017**, *32*, 30–38.
8. Jamil, K.; Alam, M.; Hadi, M.A.; Alhekail, Z.O. A multi-band multi-beam software-defined passive radar. Part I: System design. Radar 2012; , 2012; pp. 64–67.
9. Jamil, K.; Alam, M.; Hadi, M.A.; Alhekail, Z.O. A multi-band multi-beam software-defined passive radar. Part II: Signal processing. Radar 2012; , 2012; pp. 72–75.
10. Tseng, F.I.; Cheng, D.K. Optimum scannable planar arrays with an invariant sidelobe level. *Proc. IEEE* **1968**, *56*, 1771–1778.
11. Saeidi-Manesh, H.; Karimkashi, S.; Zhang, G.; Doviak, R.J. High-isolation low cross-polarization phased-array antenna for MPAR application. *Radio Sci.* **2017**, *52*, 1544–1557.
12. Saeidi-Manesh, H.; Zhang, G. Low cross-polarization, high-isolation microstrip patch antenna array for multi-mission applications. *IEEE Access* **2018**, *7*, 5026–5033.
13. Saeidi-Manesh, H.; Zhang, G. High-isolation, low cross-polarization, dual-polarization, hybrid feed microstrip patch array antenna for MPAR application. *IEEE Trans. Antennas Propag.* **2018**, *66*, 2326–2332.
14. Rocca, P.; Oliveri, G.; Mailloux, R.J.; Massa, A. Unconventional phased array architectures and design methodologies – A review. *Proc. IEEE* **2016**, *104*, 544–560.
15. Cheng, D.K. Optimization techniques for antenna arrays. *Proc. IEEE* **1971**, *59*, 1664–1674.
16. Kim, Y.; Elliott, R. Extensions of the Tseng–Cheng pattern synthesis technique. *J. Electromagn. Waves Appl.* **1988**, *2*, 255–268.
17. Elliot, R.S. *Antenna Theory and Design*; John Wiley & Sons, 2006.
18. Balanis, C.A. *Antenna Theory – Analysis and Design*; John Wiley & Sons, Inc, 2005.
19. Mailloux, R.J. *Phased Array Antenna Handbook*; Artech House, 2005.
20. Waterhouse, R. *Microstrip Patch Antennas: A Designer's Guide*; Springer Science & Business Media, 2013.

21. Mishra, P.K.; Jahagirdar, D.R.; Kumar, G. A Review of Broadband Dual Linearly Polarized Microstrip Antenna Designs with High Isolation [Education Column]. *IEEE Antennas Propag Mag* **2014**, *56*, 238–251. doi:10.1109/MAP.2014.7011064.
22. Ghorbani, K.; Waterhouse, R. Dual polarized wide-band aperture stacked patch antennas. *IEEE Trans. Antennas Propag.* **2004**, *52*, 2171–2175. doi:10.1109/TAP.2004.832484.
23. SIMULIA CST Studio Suite, Dassault Systemes. (2023).
24. Pozar, D. The active element pattern. *IEEE Trans. Antennas Propag.* **1994**, *42*, 1176–1178. doi:10.1109/8.310010.